Finding Clusters in SZ Surveys

Chris Vale [a,1], Martin White [a,b,2]

[a] *Department of Physics, University of California, Berkeley, CA, 94720*

[b] *Department of Astronomy, University of California, Berkeley, CA, 94720*

Abstract

We use simulated maps to investigate the ability of high resolution, low noise surveys of the CMB to create catalogues of Clusters of galaxies by detecting the characteristic signature imprinted by the Sunyaev Zeldovich effect. We compute the completeness of the catalogues in our simulations for several survey strategies, and evaluate the relative merit of some Fourier and wavelet based filtering techniques.

Key words: Cosmology, Large-Scale structures, Theory
PACS: 98.65.Dx, 98.80.Es, 98.70.Vc

1 Introduction

Future measurement of the distribution and number density of clusters of galaxies will place increasingly important constraints on the nature of the universe we live in (e.g. Bahcall et al., 1999; Rosati, Borgani, & Norman, 2002; Voit, 2004), and is a major science goal of upcoming surveys such as SZA [3], APEX-SZ [4], the South Pole Telescope (SPT [5]) and the Atacama Cosmology Telescope (ACT [6]) These surveys will map the millimeter and sub-millimeter sky with unprecedented power and resolution, which will enable the construction of a catalogue of clusters detected through the thermal Sunyaev Zel'dovich effect (SZE) (Sunyaev & Zel'dovich, 1972, 1980, for recent reviews see Rephaeli 1995; Birkinshaw 1999; Carlstrom, Holder, & Reese 2002) In this paper, we

[1] E-mail: cvale@astro.berkeley.edu
[2] E-mail: mwhite@astro.berkeley.edu
[3] http://astro.uchicago.edu/sza/
[4] http://bolo.berkeley.edu/apexsz/
[5] http://astro.uchicago.edu/spt/
[6] http://www.hep.upenn.edu/∼angelica/act/act.html

examine different survey strategies and signal processing methodologies to enhance this effort.

The imprint of the SZE on the cosmic microwave background (CMB) is an integrated effect from the time of last scattering to the present era, and as such the SZE signal suffers from projection effects due to other objects along the line of sight. This introduces non-linear complications to our signal processing efforts, and makes it impossible to conclusively determine the best method by analytic means alone. We therefore test and compare three promising filtering techniques: discrete wavelets, continuous wavelets, and Fourier methods. These are applied to mock SZ maps for several different survey strategies, and results for the different strategies and filters are computed.

The mock SZ maps are created using an N-body simulation of sufficient volume to be a fair sample of the universe. Due to the current uncertainty in both the magnitude of the SZE and of relevant astrophysical foregrounds, a detailed modeling of the signal and noise is not currently possible. However, some of the complications that will be encountered by actual surveys, such as confusion due to projection effects, irregularly shaped sources, maps with edges and holes, and spatially varying noise, are included in our tests prospective filters.

The outline of the paper is as follows. We describe our simulations in Section 2 and our filtering schemes in Section 3. We then present our results in the context of various survey scenarios and signal processing techniques in Section 4, and discuss our conclusions in Section 5.

2 Simulating the SZE

Since we use the method outlined in Schulz & White (2003) to create maps of the SZE, we provide only a brief description here. The maps are created from a large volume, high resolution N-body simulation containing a fair sample of the universe, for a flat ΛCDM cosmology with $\Omega_m = 0.3$, $\Omega_b h^2 = 0.02$, $h = 0.7$, and $\sigma_8 = 1$. We use a semi-analytic model, in which baryonic matter traces the dark matter in our clusters, in order to include the gas physics responsible for the SZE. This assumption is likely to be a good approximation everywhere except at the cluster cores, which will not be resolved by the surveys considered here. We identify clusters in the N-body simulation using a friends-of-friends (FOF) algorithm (Davis et al., 1985) with a linking length $b = 0.15$ times the mean interparticle spacing. The mass contained by hot gas is set to Ω_b/Ω_m of the total, and each cluster is set to be isothermal at a temperature given by

$$\frac{k_B T}{keV} \sim \left(\frac{H(z)M}{10^{15}h^{-1}M_\odot}\right)^{2/3} \qquad (1)$$

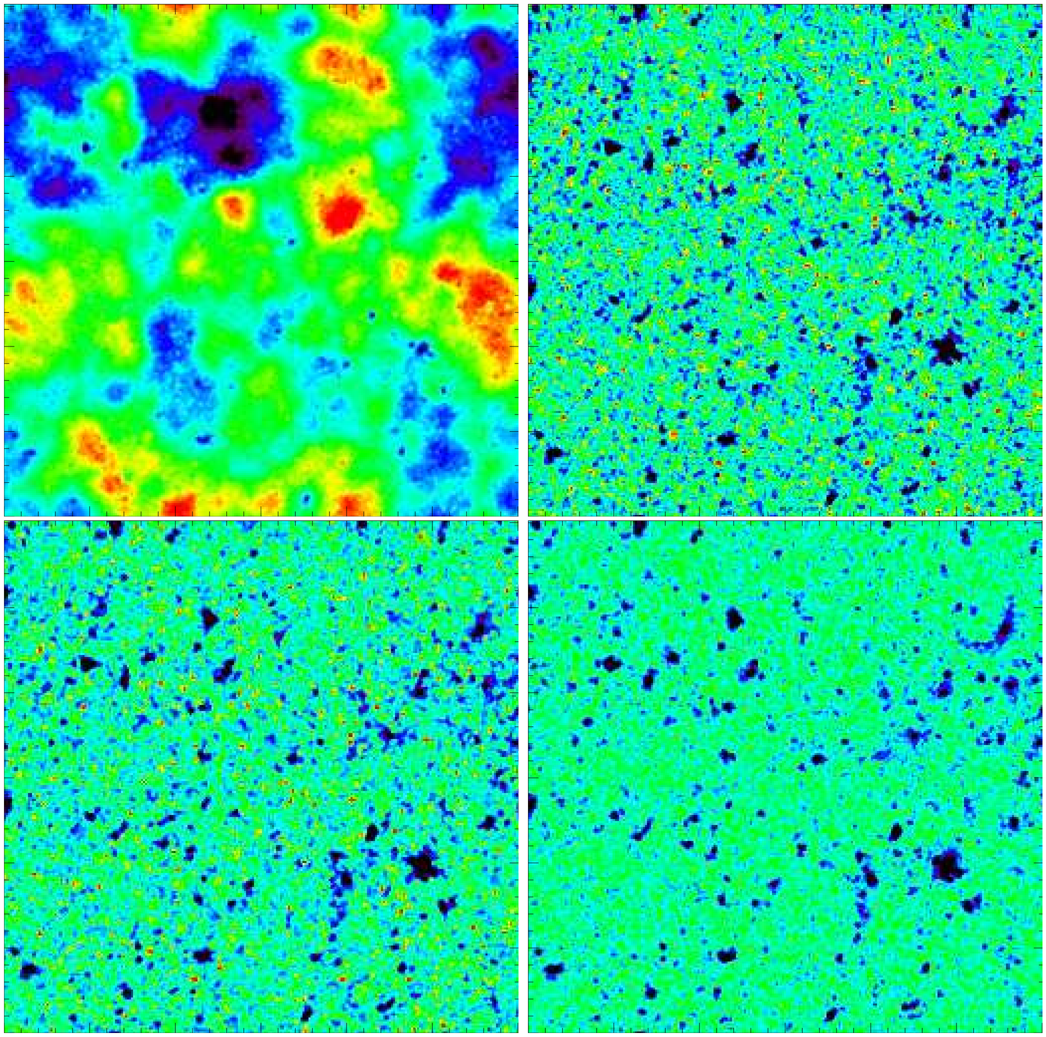

Fig. 1. An example of the maps before filtering. The full map (top left) includes the SZE signal (which shows up as cold spots on the map) and all sources of "noise". Since the signal is overwhelmed by the primary CMB on the angular scale shown here, we display the same map without the CMB (top right), but still including point source and instrument noise. The relative importance of these two effects can be seen in the bottom maps, where we have displayed the SZE with point sources but no instrument noise (left) and vice versa (right). The maps are $3° \times 3°$ and contain 1024^2 pixels, rebinned to 256^2 for display. The color scale of the maps is linear, and span 100μK, except for the map including the primary CMB, which spans 500μK. This particular map is made at 150 GHz for a 12 meter dish, assuming 10μK-arcmin of instrument noise, and with point source contributions near the high end of the expected magnitude.

where $H(z)$ is the hubble parameter. This effectively reproduces the results of the hydrodynamic simulations of White, Hernquist & Springel (2002). The normalization has been set to pass through the lower envelope of the CBI deep field (Mason et al., 2003) and through the BIMA point (Dawson et al., 2001) on small angular scales. We generate Compton-Y maps by projecting along each line of sight, so that

$$y = \int \sigma_T n_e \frac{k_B T}{m_e c^2} dl \tag{2}$$

where σ_T is the Thompson scattering cross section, n_e is the electron number density, and m_e is the electron mass. The temperature fluctuation for a given frequency ν is related to the Y-maps by

$$\frac{\Delta T}{T} = y \left(x \frac{e^x + 1}{e^x - 1} - 4 \right) \tag{3}$$

where $x = h\nu / k_B T_{CMB} \simeq \nu / 56.84\text{GHz}$ is the dimensionless frequency. Ten maps are made in this manner (see Figure 1 for an example), each with 1024^2 pixels and 3° on a side. These are not as accurate as those produced using full hydrodynamic simulations, but they allow us to probe a larger volume and therfore provide a better sample of large clusters situated in their proper cosmological context.

In the absence of perfect spectral information, confusion due to the primary CMB temperature anisotropy and to point sources may impede the detection of clusters. We simulate the former using realizations of a Gaussian random fields convolved with the CMB power spectrum computed using CMBfast (Seljak & Zaldarriaga, 1996). We then add radio and infrared (IR) point sources to the maps using the model of White & Majumdar (2004). For radio sources, this is a fit to the Q-band data of WMAP (Bennett et al., 2003), while IR sources are fit using the 350 GHz observations of Borys et al. (2003) with the Submillimeter Common User Bolometer Array (SCUBA: Holland et al., 1999) on the James Clerk Maxwell Telescope. We note that there is substantial uncertainty in extrapolating these fits to frequencies relevant to us here, so we examine two different extrapolations likely to span the magnitude of the effect.

The maps are then smoothed with a Gaussian beam, and Gaussian white noise is added. Although we have ignored many effects which may be important in real world observations (such as offsets, drifts, and atmosphere), we treat the maps as completed and ready for signal processing.

3 Filtering methods

In this section, we describe the filters we use to process the simulated maps discussed in Section 2. These maps have a complex structure which makes it impossible to analytically determine the best filter to aid our efforts at cluster identification, so we explore several different methods. We begin by describing

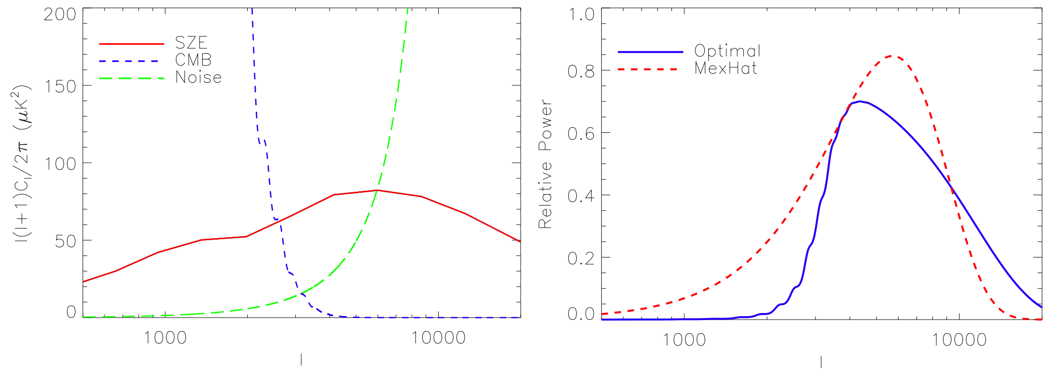

Fig. 2. (Left) The expected magnitude of the SZE, the CMB, and instrument noise for a fiducial $10\mu K$ per $1'$ beam survey, shown here in Fourier space. The SZE signal exceeds both the noise and CMB on roughly arcminute scales. (Right) The optimal and mexican hat filters in Fourier space. The filters are wedge shaped band pass filters, designed to pass scales where the SZE is large relative to the CMB and instrument noise.

the optimal Fourier based filter of Tegmark & de Oliveira-Costa (1998), then briefly describe filtering in the discrete wavelet basis, where we focus on the Daubechies wavelet family (Daubechies, 1992). Finally, we discuss filtering using the continuous mexican hat wavelet filter (see Pierpaoli et al., 2004, for more discussion of filtering with continuous wavelets).

The signal power in the SZE is expected to exceed that of the primary CMB and (for a sufficiently powerful survey) instrument noise on roughly arcminute scales (Figure 2). The optimal filter derived in Tegmark & de Oliveira-Costa (1998) is essentially a bandpass window which can be centered on the appropriate angular scale, and is therefor an obvious candidate for our purpose. This filter is azimuthally symmetric, and its radial dependence in Fourier space is

$$\tilde{\psi}_{match}(\ell) \sim \frac{e^{\theta^2 \ell(\ell+1)/2}}{C_\ell^{\rm Tot}} \tag{4}$$

where θ is the full width half max (FWHM) beam size and $C_\ell^{\rm Tot}$ is the total power spectrum of all "noise". See Figure 2 for an example of this filter appropriate for our fiducial surveys.

Wavelets have emerged as a powerful tool for signal processing (see the Appendix for a brief discussion and e.g. Mallat, 1999, for a review of wavelet signal processing). They are simultaneously (but imperfectly) localized in both real space and Fourier space, and are therefore a natural choice for processing data which possesses both real space and Fourier space correlations, such as we expect from our fiducial surveys. We employ the wavelet transform algorithm outlined in Press et al. (1992), and although we focus on the Daubechies wavelets, we note that we have also explored the Coiflet, Symlet, and Morlet wavelet families, and as these offer essentially the same results as the

Daubechies wavelets, we do not discuss them further.

To generate our filter, we follow Pen (1999) and estimate the expected signal given data $\langle S|D\rangle$ for each coefficient in the wavelet transform. This amounts to Wiener filtering in the limit of Gaussian noise and Gaussian signal, and to thresholding for highly non-Gaussian signal distributions, such as unsmoothed point sources. This approach is likely to be superior (in the sense of minimizing the least squared error in the reconstruction) if the signal or noise include substantial non-Gaussian behavior, but requires that the signal and noise probability density functions (PDF) be known. Although Pen (1999) suggests computing $\langle S|D\rangle$ directly from the non-Gaussian behavior of the observed maps, we find that the procedure outlined there is subject to numerical artifacts due to the finite size of sky in our simulations, so we compute this function directly from our 10 input signal maps. This will not be possible for real surveys, and so should be considered an upper limit to the performance of the technique.

We implement a third class of filter, the continuous wavelet filter, using the mexican hat wavelet transform (e.g. Cayon et al., 2000; Maisinger, Hobson, & Lasenby, 2004). The continuous wavelet transform $W(a,b)$ of a one dimensional function $f(x)$ is a real space convolution of $f(x)$ with a "mother wavelet" $\psi(x)$

$$W(a,b) = \int dx f(x) \frac{1}{\sqrt{a}} \psi\left(\frac{x-b}{a}\right) \tag{5}$$

where a and b are the scale and position parameters. This convolution is normally performed as a multiplication in the Fourier domain, so that $\tilde{W} = \sqrt{a}\tilde{f}(\ell)\tilde{\psi}(a\ell)$, where the tilde denotes the Fourier transform. The mexican hat wavelet is the second derivative of a Gaussian, so that its Fourier transform is

$$\tilde{\psi}_{mex}(a\ell) \sim (a\ell)^2 \exp\left[-\frac{(\mathrm{a}\ell)^2}{2}\right] \tag{6}$$

Like the optimal filter, the continuous wavelet transform is essentially a filter in Fourier space, as can be seen in the side by side comparison in Figure 2.

In the next section, we demonstrate the use of these filters on the simulated maps described in Section 2 for various survey strategies.

4 Results

In this section, we examine the maps after application of the filters described in Section 3. As can be seen in the examples shown in Figure 3, the three filters clearly all succeed in improving signal to noise, with large structures in

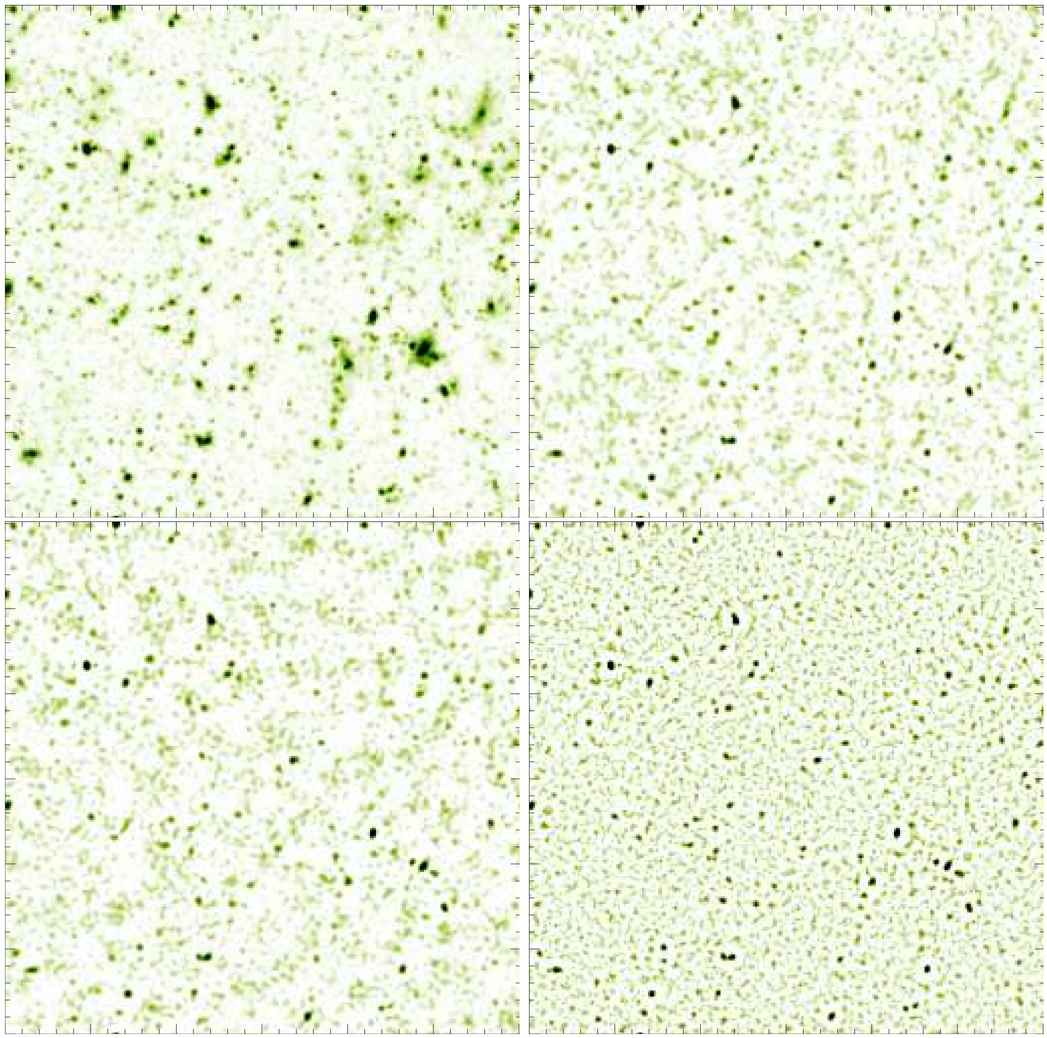

Fig. 3. The input SZE (top left) and the filtered maps for the discrete Daubechies wavelet filter (top right), the mexican hat continuous wavelet filter (bottom left), and for the optimal Fourier filter (bottom right). The color scale is linear, and structures less than 1σ of the noise have been suppressed for visual clarity.

the filtered maps all corresponding to massive clusters. We quantify the level of this success using the peak finding algorithm of Schulz & White (2003), and conclude that for the surveys we consider here, the optimal filter performs at least as well as the wavelet based filters for creating complete, efficient surveys of clusters. We then examine cluster finding in the context of several survey strategies.

Of the three filtered maps shown here, the one created using the discrete wavelet (specifically, Daub6) "$\langle S|D\rangle$" technique described in Section 3 best reconstructs the input SZE signal in the sense of minimizing the least squared error of the reconstruction. However, this reconstruction does not do as well at creating complete, efficient surveys of clusters. This is because a large fraction of the improved signal recovery is associated with a few giant clusters.

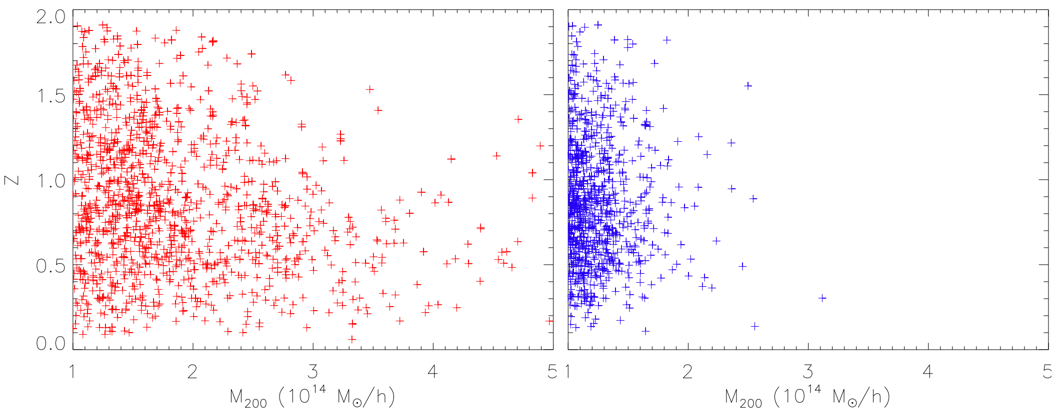

Fig. 4. Clusters found (left) and missed (right) as a function of mass and redshift for our fiducial 10 μK per arcminute beam survey. The survey size is 90 square degrees, and we have required a 75% detection efficiency for clusters of mass above 10^{14} $M_{\odot}$.

Since these produce enormous signal, they are easy to find, regardless of the filter, and improving their reconstruction does not aid in the completeness of the catalogue. However, these clusters have signal on relatively large angular scales, so that the "$\langle S|D\rangle$" technique smooths the maps more than is optimal for finding smaller clusters at the threshold of detection. Although this can be accounted for by eliminating the large clusters from consideration when formulating the filter, the result is to simply scale the signal by a constant at each level, so that the smaller cluster signal is effectively in the Wiener filter limit. Although we do not show them here, we have also considered maps with holes, rough edges, and spatially varying noise. The wavelet filter performs better in this context than the other filters for extreme conditions, but there is no detectable advantage for realistic assumptions.

The mexican hat filter and the optimal filter of Tegmark & de Oliveira-Costa (1998) perform about equally well. In fact, we find that the primary CMB anisotropy is easy to separate morphologically from the SZE for the small beam sizes we consider here, and any reasonable hi-pass filter can be used for this task. If the two filters are then set to be roughly the same on small angular scales, then they perform about equally well at cluster finding. In particular, we find that for clusters which are smaller than the beam of the survey, simply smoothing the noisy maps by the beam performs best for small scale filtering.

We use two methods to identify signal peaks in the filtered maps. The first simply flags local maxima, while the second computes the total flux in all pixels surrounding (and including) the local maxima which are greater than one quarter the peak value. Since the choice of method does not significantly alter our results, the results presented here are for the simpler local maxima technique unless stated otherwise.

Once we have identified signal peaks in the maps, we compare these to a list

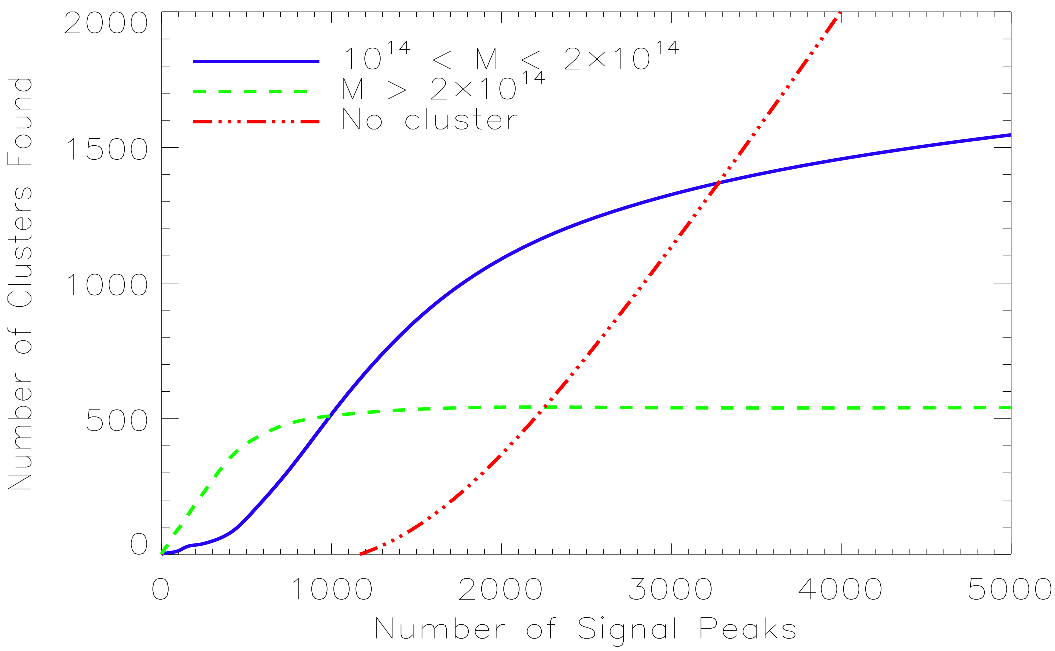

Fig. 5. The number of massive clusters associated with the 5000 largest peaks in the filtered signal for our 10 maps, shown here in descending order of signal strength, for our fiducial 10 μK per arcminute beam survey. The largest signal peaks are always associated with a cluster. However, noise and projection effects cause substantial scatter in the mass-observable relation. In the small signal regime, this scatter begins to dominate, so that many smaller peaks are not associated with a cluster of mass $M > 10^{14}$ $M_\odot$. We note that there are a total of 1900 clusters in the (solid) mass range of $10^{14} < M < 2 \times 10^{14}$ $M_\odot$ and 550 of (dashed) mass $M > 2 \times 10^{14}$ $M_\odot$ in our simulation.

of clusters in our simulation. As can be seen in Figure 4, massive clusters are nearly always identified using this method, while no particular dependence on redshift is evident. Also, large signal peaks are nearly always associated with a cluster (Figure 5), although noise and projection effects cause substantial scatter in the mass-observable relation. The efficiency of the survey (that is, the chance that a signal peak corresponds to a cluster) is therefor nearly 100% for large peaks.

We now turn our attention to survey strategy, where we examine the use of multiple vs single frequency measurements. Although the primary CMB anisotropy is not a serious contaminant, contributions from point sources are non-negligible. Spectral information can alleviate this issue, but at the price of either reduced signal to instrument noise, or less sky coverage, per unit of telescope time. If only a single frequency is used, then point source contributions must be considered in addition to signal strength, instrument noise, and beam size.

To investigate this issue, we begin with a fiducial survey at 150 GHz for a 12 meter dish (roughly a $0.'8$ beam at 150 GHz) and 10μK-arcmin instrument

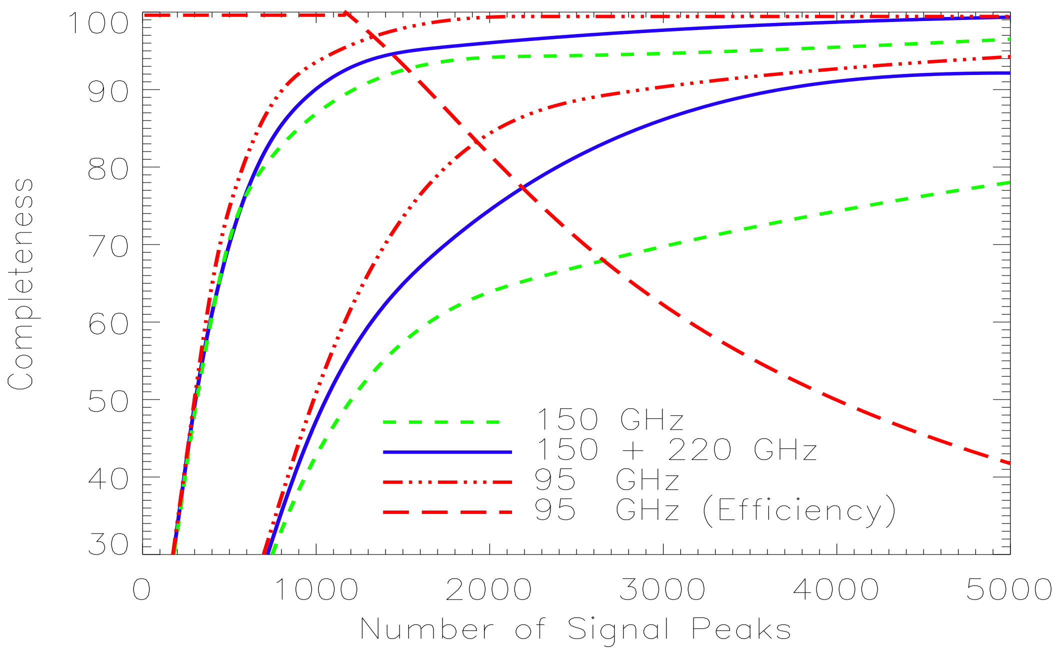

Fig. 6. Completeness of clusters detected above a mass threshold for three survey strategies as a function of the number of signal peaks included in the analysis. The upper family of curves is the completeness for clusters of mass greater than 2.0×10^{14} M$_\odot$, while the lower family is for clusters of mass less than this but greater than 1.5×10^{14} M$_\odot$. The efficiency for a threshold mass of 10^{14} M$_\odot$ for one survey is also shown. The totals are derived from ten $3° \times 3°$ simulated maps.

noise over our 90 square degrees of simulated sky. As expected, this survey does well at cluster identification in the absence of point sources. However, including them substantially worsens the result (Figure 6), even for a level at the low end of the expected confusion noise, and a deeper integration at the same frequency only marginally improves the outcome. A better result is achieved by combining the 150 GHz survey with a 220 GHz observation and differencing the results to remove the point source contribution. Although the 220 GHz channel contains no signal and is noisier than the 150 GHz channel (we assume $\sim 15\mu$K-arcmin for the same integration time), the effective signal to instrument noise is only marginally worse. This is because the point source contribution is roughly twice as large at 220 GHz as it is at 150 GHz, so that (roughly speaking) the point source elimination is accomplished by including only half the noise of the instrument noise at 220 GHz. Added in quadrature, this is effectively a 12μK-arcmin survey.

An alternative strategy is explored in the form of a single frequency survey at 95 GHz. This offers the advantage of a larger signal and lower point source contamination, but is noisier (we assume 17μK-arcmin for equal integration time) and has a larger ($\sim 1.'3$) beam. This results in improved detections, and although the level of improvement depends upon the model of point source confusion assumed, this survey strategy is superior in our simulations for the

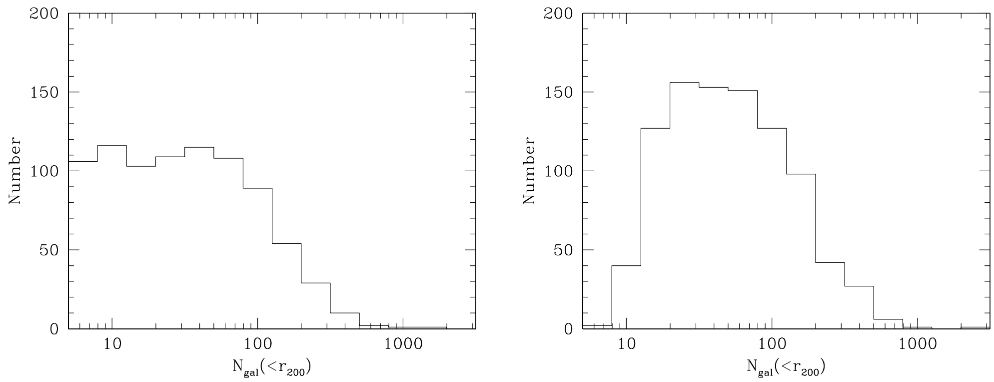

Fig. 7. The number of galaxies brighter than (left) R = 24 and (right) R = 25 within the virial radius of clusters in our sample with mass greater than $10^{14}M_{\odot}$ and at redshift $Z < 1$. The number within the core region, where the contrast against the background is highest, is about 10% of $N_{gal}(< r_{200})$.

models we have considered here. We have not accounted for clustering of point sources, which may change this result.

Finally, we note that optical and near-IR emission is still the least expensive way of measuring cluster redshifts, and that redshift information is crucial to the physical interpretation of the cluster sample. We use the method outlined in White (2003) to provide a rough estimate (Figure 7) of the number of galaxies brighter than $R = 24$ and $R = 25$ within the virial radius of the clusters detected (at 75% efficiency above mass $M > 10^{14}\ M_{\odot}$ and at redshift $Z < 1$) in our fiducial survey. The number in the core region, where the contrast against the background is the highest, will obviously be smaller. If the galaxies follow the mass, approximately 20% of the galaxies lie within the break radius ($0.2r_{200}$) and 8% within the core radius ($0.1r_{200}$). Although the results we show here are for clusters at redshift $Z < 1$, the results for higher redshifts will clearly be somewhat worse. Optical follow up will no doubt be an integral but challenging complement to an SZE cluster survey similar to that discussed here.

5 Conclusions

Measurement of the CMB using the unprecedented combination of power, resolution, and sky coverage expected in upcoming surveys will return a wealth of information, including high resolution detections in the SZE sky sufficient to provide enormous catalogues of galaxy clusters. We have studied the use of several filtering techniques to aid the cluster identification process, and evaluated the likely detection of clusters using simulated maps of the CMB. We note that while further signal analysis will be required to optimally measure cluster properties, we have not addressed that issue here.

We have tested three filter techniques, using Fourier methods, continuous wavelets, and discrete wavelets, and have found that all of these can be efficiently used to enhance the signal to noise in our maps. Although the discrete wavelets perform better under some extreme conditions, we find that each of these techniques may be used effectively to aid cluster detection.

We have also examined the success of survey strategies in creating complete catalogues of clusters for a given mass threshold. We find that the primary CMB anisotropy is not an important source of noise for the high resolution surveys we have considered here, but that point sources may in some cases be more important than instrument noise. Accordingly, multi-frequency measurements are likely required if the sky is probed in frequency bands where point sources are large relative to the signal strength. A single frequency band may be used effectively if the band center is selected at a frequency where point source contamination is not expected to overwhelm the signal. We note that the magnitude of the point source confusion and clustering are not as yet well measured at frequencies relevant to us here, so that we are dependent upon models for our results.

A well understood, nearly complete catalogue of massive clusters over a large fraction of the sky would be a major achievement for cosmology, and will likely be available in the near future as powerful surveys begin operation. The road to optimizing the results includes a determination of the best survey strategies and signal processing techniques, and in this endeavor, simulations can play an important role. We have made the raw maps, along with some auxiliary data products, freely available to the community at http://mwhite.berkeley.edu/ in the hope that they will be useful in taking the next step.

CV would like to thank J.D. Cohn, Tom Crawford, Steve Myers, and Wayne Hu for useful discussions. The simulations used here were performed on the IBM-SP at the National Energy Research Scientific Computing Center. This research was supported by the NSF and NASA.

A Appendix: Wavelets

In this section, we provide a brief discussion of discrete wavelets to orient the reader (see e.g. Mallat, 1999, for a more substantial introduction to wavelet signal processing). To get a feel for wavelets, let us consider the first order Daubechies wavelet, Daub1, also called the Haar wavelet. In one dimension, the first level (not to be confused with order) Daub1 transform involves computing the two pixel average $\mathbf{a}$ and difference $\mathbf{d}$ of a signal $\mathbf{f} = (f_1, f_2, \ldots, f_N)$,

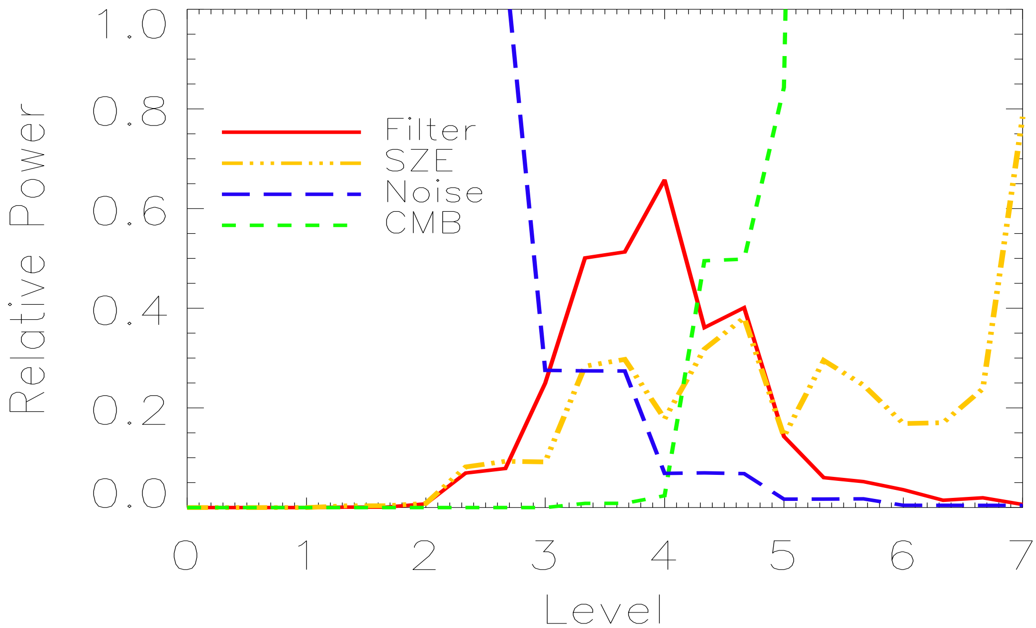

Fig. A.1. The SZE signal is comparable to the level of confusion from the primary CMB and instrument noise on intermediate angular scales. Here, we display this effect for the 6^{th} order Daubechies wavelet, and the resulting level dependent filter.

so that the elements a_m of $\mathbf{a}$ are defined by

$$a_m = \frac{f_{2m-1} + f_{2m}}{\sqrt{2}} \tag{A.1}$$

and similarly for $\mathbf{d}$, but with a minus sign on the right hand side of Eq.(A.1). Like all discrete wavelet transforms, the Daub1 transform decomposes a signal into two subsignals half the length of the original: a running average $\mathbf{a}$ called the trend, and a running difference $\mathbf{d}$ called the fluctuation. Note that this transform is linear, invertible, and preserves the total sum of squares of the pixels (the latter is often called "conservation of energy" in wavelet parlance). For higher order transforms, the trend and fluctuation subsignals are no longer simple averages and differences (for example, the Daub2 transform uses a four pixel linear fit rather than a two pixel average), but the basic idea is the same.

An essential component of wavelet based analysis is the simultaneous processing of data at multiple scales. This "Multi-Resolution Analysis" (MRA) is implemented by a hierarchical application of the wavelet transform on the data, so that the first level transform, which probes the smallest physical (and highest frequency) scales, is applied to the original signal. The second level transform is then computed by taking the wavelet transform of the first level trend signal, and so on, so that for an $\mathrm{n^{th}}$ level transform, the result is a single trend $\mathbf{a^n}$ and n fluctuations $\mathbf{d}^1, \mathbf{d}^2, \ldots, \mathbf{d}^n$.

Most discrete wavelet filtering techniques are based on the "thresholding"

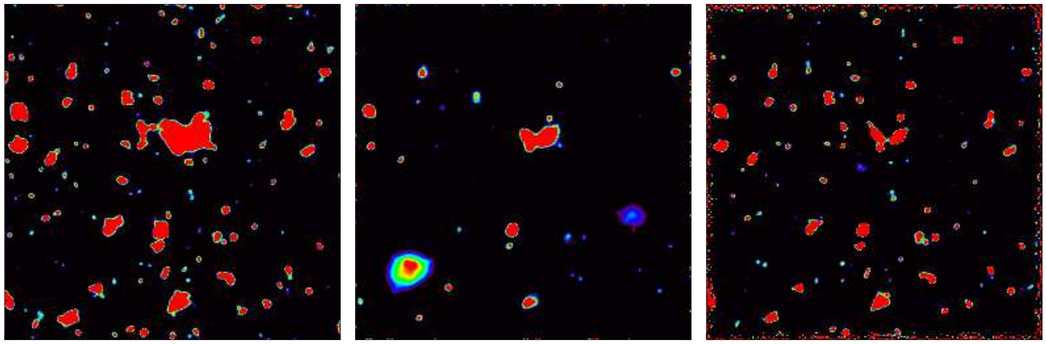

Fig. A.2. The input SZE (left) and the filtered maps for the optimal filter (center) and the discrete Daubechies wavelet filter (right), in an extreme case where the noise level in the maps is varied by a factor of several hundred. The recovered maps shown here are in low noise regions, and in this case, the localized nature of the wavelet filter allows for a substantial improvement in the reconstruction. For realistic noise, this advantage is not detected in our maps.

modality, where wavelet coefficients with an absolute value less than a chosen threshold value are discarded. This is effective when the signal is much larger than the noise, and when the goal is to recover an image which is visually appealing to the human eye. An approach more suited to our purpose is to attempt to reconstruct the signal with a minimum least squared error. For a Gaussian signal and uncorrelated Gaussian noise, this implies a Wiener filter in Fourier space. The equivalent filter in wavelet space can be constructed by estimating the energy of the signal divided by the data for each level and scaling the transformed data at each level by this ratio. The required estimate of the signal energy can be obtained either using simulations, or directly from the data if the noise is well understood. We show an example of this filter for the Daub6 wavelet in Figure A.1.

One simple use of a wavelet filter is to account for spatially varying noise. If the statistical properties of the noise is known as a function of position, then a wavelet filter can adjust to accommodate this in a more natural way than filters with no localized spatial properties. We show an example of this in Figure A.2 vs. the optimal filter, for an extreme case where the noise fluctuates by a factor of several hundred in the maps. Although the reconstruction is notably improved in this highly artificial case, no improvement was evident in our maps for more realistic noise.

References

Bahcall N., Ostriker J., Perlmutter S., Steinhardt P., 1999, Science, 284, 1481
Bennett C.L., et al., 2003, ApJS, 148, 97 [astro-ph/0302208]
Birkinshaw M., 1999, Phys. Rep., 310, 98

Borys C., Chapman S.C., Halpern M., Scott D., 2003, MNRAS, 344, 385 [astro-ph/0305444]
Carlstrom J., Holder G., Reese E., 2002, ARAA, 40, 643
Cayon L., et al., 2000, MNRAS, 315, 757
Daubechies I., 1992, Ten Lectures on Wavelets, SIAM, Philadelphia
Davis M., Efstathiou G., Frenk C.S., White S.D.M., 1985, ApJ, 292, 371
Dawson K.S., Holzapfel W.L., Carlstrom J.E., Joy M., LaRoque S.J., Reese E.D., 2001, ApJ, 553, L1
Holland W.S, et al., 1999, MNRAS, 303, 659
Maisinger K., Hobson M.P., Lasenby A.N., 2004, MNRAS, 347, 339 [astro-ph/0303246]
Mallat S., 1999, A Wavelet Tour of Signal Processing, Academic Press
Mason B.S., et al., 2003, ApJ, 591, 540 [astro-ph/0205384]
Pen U., 1999, Phil.Trans.Roy.Soc.Lond. A357, 2561 [astro-ph/9904170]
Pierpaoli E., Anthoine S., Huffenberger K., Daubechies I., 2004, submitted to MNRAS [astro-ph/0412197]
Press W.H., Teukolsky S.A., Vetterling W.T., Flannery B.P., 1992, Numerical Recipes in C, 2nd edition, Cambridge University Press
Rephaeli, Y., 1995, ARA&A, 33, 541
Rosati P., Borgani S., Norman C., 2002, ARA&A, 40, 539
Schulz A., White M., 2003, ApJ, 586, 723 [astro-ph/0210667]
Seljak U., Zaldarriaga M., 1996, ApJ, 469, 437
Sunyaev R.A., Zel'dovich Ya. B., 1972, Comm. Astrophys. Space Phys., 4, 173
Sunyaev R.A., Zel'dovich Ya. B., 1980, ARA&A, 18, 537
Tegmark M., de Oliveira-Costa A., 1998, ApJ, 500, L83 [astro-ph/9802123]
Voit G.M., 2004, Rev. Mod. Phys. (in press) [astro-ph/0410173]
White M., 2003, ApJ, 597, 650 [astro-ph/0302371]
White M., Hernquist L., Springel V., 2002, ApJ, 579, 16 [astro-ph/0205437]
White M., Majumdar S., 2004, ApJ, 602, 565 [astro-ph/0308464]